

See discussions, stats, and author profiles for this publication at: <https://www.researchgate.net/publication/255713095>

The Silane Radical Cation: A Theoretical Account on the Jahn–Teller Effect at a Triple Degeneracy.

ARTICLE in THE JOURNAL OF PHYSICAL CHEMISTRY A · AUGUST 2013

Impact Factor: 2.69 · DOI: 10.1021/jp404393n · Source: PubMed

CITATIONS

3

READS

32

2 AUTHORS:

[Tanmoy Mondal](#)

BITS Pilani, K K Birla Goa Campus, India

14 PUBLICATIONS 76 CITATIONS

SEE PROFILE



[Antonio J. C. Varandas](#)

University of Coimbra

382 PUBLICATIONS 6,747 CITATIONS

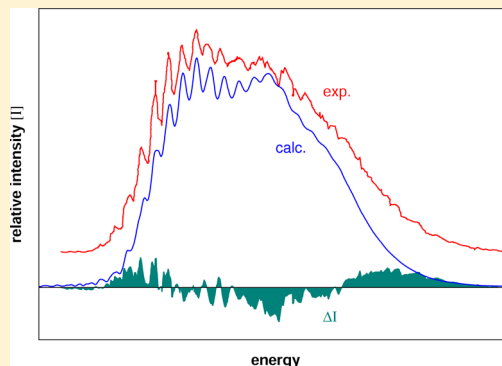
SEE PROFILE

Silane Radical Cation: A Theoretical Account on the Jahn–Teller Effect at a Triple Degeneracy

T. Mondal and A. J. C. Varandas*

Departamento de Química, Universidade de Coimbra, 3004-535 Coimbra, Portugal

ABSTRACT: An ab initio quantum dynamics study is performed to examine the complex nuclear motion underlying the first photoelectron band of the silane molecule due to Jahn–Teller distortion via $T_2 \otimes (e+t_2+t_2)$ coupling. The problem is investigated by employing a quadratic vibronic coupling model for the Hamiltonian. All sheets of the required potential energy surface are established through extensive electronic structure calculations using the multireference configuration-interaction method. They cover at most two dimensions of the full 9D coordinate space, with the parameters defining the model Hamiltonian being determined by a least-squares fitting procedure. The results are compared with the available experimental data and discussed in relation to those obtained for the methane radical cation. The quadratic couplings of Jahn–Teller active vibrational modes are found to have a crucial role on the irregular vibronic structure, intensity of the spectral excitations, and overall width of the first photoelectron band of the title molecule. The impact of large amplitude motions on the vibronic structure and dynamics of the first photoelectron band has also been examined by varying their linear coupling parameters up to $\pm 10\%$.



INTRODUCTION

The Jahn–Teller (JT) effect^{1–8} is an important manifestation of vibronic coupling (entanglement of electronic and nuclear motions), which plays a key role in the structure and dynamics of symmetric nonlinear molecular systems in a degenerate electronic state. Beyond the much studied $E \otimes e$ JT effect (and references therein),^{1–8} the coupling of a triply degenerate electronic state (T_2) with a doubly degenerate (e) and/or triply degenerate (t_2) vibrational modes exhibiting the so-called $T_2 \otimes (e+t_2)$ JT effect^{3,5,9–15} is a widespread phenomenon in systems with cubic symmetry. In particular, the radical cations of group IV hydrides (XH_4^+ at their initial T_d symmetry) provide examples of strong $T_2 \otimes (e+t_2)$ JT coupling.^{14–17} Indeed, with a view to examine the JT effect^{1–8} on a triply degenerate electronic state, we have recently performed an extensive study^{18,19} of the methane radical cation (CH_4^+). Note that this is the simplest organic radical cation possessing a 3-fold degenerate electronic ground state (\tilde{X}^2T_2) with JT active vibrational modes of e and t_2 symmetry, thus defining the prototype system for the multimode $T_2 \otimes (e+t_2+t_2)$ JT problem. However, such an apparently simple system is quite challenging, with an accurate theoretical treatment being far from trivial. Additionally to the multimode JT coupling effect, the intricacy arises due to the pathologically flat lowest adiabatic potential energy surface (PES) of CH_4^+ near the C_{2v} minimum where many symmetry-related stationary points occur.^{20,21} In turn, CH_4^+ is a highly fluxional species in its ground electronic configuration.^{20–22} As a result, it is a long-standing challenge for theory in molecular photoelectron spectroscopy. In previous papers,^{18,19} we have suggested and examined for the first time a qualitative way to assess such a problem by varying the gradient of the adiabatic PESs associated

with the large amplitude motions, because they should be responsible for the above fluxional character. Subsequently, we investigated their role on the vibronic structure and dynamics of the CH_4 first photoelectron band. Similarly, the silane radical cation (SiH_4^+) of group IV hydrides should pose all the above challenges, including the triple T_2 degeneracy in the ground electronic state. Thus, it undergoes the JT effect, which may have a pivotal role on the structure and dynamics of its first photoelectron band. Not surprisingly, perhaps, much less is known theoretically about it.

The growing attention on the properties of silane (SiH_4) arises due to its practical importance in the semiconductor industry,²³ as well as the role played in the systematics of the group IV hydrides. Moreover, SiH_4 is an important system due to its astrophysical relevance, because 13 absorption lines have been observed in the gas surrounding the IRC +10216 star with the NASA Infrared Telescope Facility.²⁴ The vacuum ultraviolet (VUV) radiation sources for recording the spectra of SiH_4 below first ionization potential^{25,26} and the extreme ultraviolet (XUV) radiation sources for recording the spectra above first ionization potential^{25,27–30} have both been used to understand the dissociation processes of this molecule at different excited states. The theoretical investigation by means of ab initio calculations predict a high activation barrier of decomposition (~ 4.7 eV) for the ground state.³¹ Nevertheless, the activation barriers at excited

Special Issue: Structure and Dynamics: ESDMC, IACS-2013

Received: May 3, 2013

Revised: June 29, 2013

states leading to $\text{SiH}_2 + \text{H}_2$ and $\text{Si} + 2\text{H}_2$ are significantly lower than those for the ground state.^{32,33} Additionally, an unambiguous understanding of the ionization dynamics of SiH_4 (an important pathway of SiH_4 in plasma dry etching processes) is lacking. Indeed, mass spectroscopic studies confirm the abundance of various ionic species of SiH_4 , e.g., SiH_3^+ , SiH_2^+ , SiH^+ , and Si^+ , as the primary cations in silane plasmas. In particular, Lampe and co-workers^{34,35} have shown that SiH_3^+ is one of the most abundant ions in silane plasma, which has also been confirmed by high-resolution diode laser spectroscopy.³⁶ Despite this, the formation mechanism of SiH_3^+ and SiH_2^+ is still puzzling. In addition, there has been much debate regarding the stability of SiH_4^+ . Moreover, evidence has been gathered both for and against the existence of SiH_4^+ from various photoelectron^{37,38} and photoionization^{39–41} experiments. Additionally, the photoelectron spectrum of SiH_4 recorded by both Pullen et al.³⁷ and Potts and Price³⁸ exhibits a broad and highly irregular vibrational structure that bears the signature of a very strong multimode JT effect.

Theoretically, the structure of SiH_4^+ has been investigated in relation to the JT distortion. Four possible structures with C_{3v} , C_s , C_{2v} , and D_{2d} symmetries have been determined. Gordon⁴² and Power et al.⁴³ found a C_{3v} minimum structure at UHF level of theory which appears to be a $\text{SiH}_3^+ \cdots \text{H}$ complex. In turn, Caballol et al.⁴⁴ studied the JT distortion in SiH_4^+ using CI level calculations and located a C_{2v} minimum structure similar to the C_{2v} one of CH_4^+ . Subsequently, Pople and Curtiss⁴⁵ have located the lowest energy structure of SiH_4^+ to be a donor–acceptor complex composed of SiH_2^+ and H_2 with C_s point group symmetry at both the UHF and MP4 levels of theory; the associated bond length for H_2 was found to be 0.794 Å. Additionally, the C_{3v} structure has been predicted to be 7.1 kcal mol^{−1} higher in energy than the C_s symmetry one. Recently, de Proft and Geerlings⁴⁶ have shown, on the basis of QCISD/cc-pVTZ calculations, that the relative energies for the D_{2d} , C_{3v} , and C_{2v} structures with respect to the C_s symmetry are 27.2, 16.4, and 9.4 kcal mol^{−1}, respectively. Although a number of ab initio calculations on the static properties of SiH_4 and SiH_4^+ molecules have been reported in the literature, little attention has been paid to the dynamic features of SiH_4^+ .

We focus therefore our attention in the present work on the mechanism of highly irregular vibronic structure and JT dynamics of the $\tilde{X}^2\text{T}_2$ electronic manifold of SiH_4^+ following the ionization of SiH_4 . Specifically, our aim is to devise a theoretical model to examine the nuclear motion underlying the vibronic structures encountered in the photoelectron band of SiH_4 . Recall that the electronic nonadiabatic coupling may have a pivotal role to reach a satisfying interpretation of the highly overlapping and complex structure of the photoelectron spectrum. Thus, the three lowest adiabatic electronic states of latter must be considered, including all nine relevant vibrational degrees of freedom. For this, a diabatic formalism will be employed, with the elements of the electronic Hamiltonian matrix being considered up to quadratic terms. They will be formed from all possible nontotally symmetric tensor convolutions involving up to quadratic combinations of the e and t_2 vibrational modes, i.e., a quadratic vibronic coupling (QVC) scheme. Additionally, an issue referring to the floppiness of the title radical cation and hence to the adequacy of the present QVC model Hamiltonian for such fluoxinal molecule will be examined. A scheme to deal with this problem, already proposed and tested in our previous investigation,¹⁹ will then be utilized. Accordingly, we first nail down the modes that are likely responsible for

floppiness and then systematically vary the associated slopes at the crossing seam. Because such a semiempirical strategy would require a mammoth investment of computational work to be optimum, only a few trials will be performed for illustrative purposes. Extensive quantum chemical calculations are also performed to derive the relevant coupling parameters of the vibronic Hamiltonian discussed in the Theoretical Framework section. Because a full-dimensional treatment of nuclear dynamics in the time-independent picture including all nine relevant vibrational modes is computationally impracticable, the task will be accomplished time-dependently via wave packet (WP) propagation using the multiconfiguration time-dependent Hartree (MCTDH) method.^{47–51} Such a propagation scheme has proven very successful, particularly in treating multistate multimode vibronic coupling problems of large dimensionalities;^{47–51} the details of the method are well documented^{47–51} and will not be reiterated. Although the final results are obtained by this method, test calculations to assign various vibrational excitations toward the partial spectra in terms of a_1 , e, and t_2 vibrational modes have also been carried out in reduced-dimensionality via a matrix diagonalization approach⁴ using the Lanczos algorithm.⁵² The diagonal elements of the resulting eigenvalue matrix give the energies of the vibronic levels and the relative intensities as calculated from the squared leading components of the Lanczos eigenvectors.⁵³ As will be shown, the theoretical findings are predicted in good accord with experimental data, revealing that the strong JT effect in SiH_4^+ ($\tilde{X}^2\text{T}_2$) primarily contributes to the highly diffuse vibronic structures of its first photoelectron band.

THEORETICAL FRAMEWORK

Vibronic Hamiltonian. The required vibronic coupling Hamiltonian to simulate the nuclear dynamics on the above-mentioned ground ($\tilde{X}^2\text{T}_2$) electronic state of SiH_4^+ is modeled in this section. This $\tilde{X}^2\text{T}_2$ electronic state undergoes JT splitting in first order when distorted from the equilibrium configuration, $\mathbf{Q} = 0$, of ground state SiH_4 along the nuclear vibrations of either e or t_2 symmetry, whereas the totally symmetric a_1 vibrational mode is tuning active within this electronic manifold.⁴ A diabatic electronic representation is employed to set up the Hamiltonian. The PESs of the three sheets of $\tilde{X}^2\text{T}_2$ electronic manifold of SiH_4^+ and their coupling surfaces are expanded via a Taylor series expansion of the electronic matrix elements in terms of dimensionless normal coordinates (e.g., Q_i for vibrational mode ν_i) of the electronic ground state ($\tilde{X}^1\text{A}_1$) of SiH_4 . The elements of the electronic matrix are considered up to second-order terms of all possible nontotally symmetric tensor convolutions that can be obtained from quadratic combinations involving the e and t_2 vibrational modes.

The present diabatic vibronic Hamiltonian on the basis of dimensionless normal coordinates (Q_i) of the vibrational modes (ν_i) is written as

$$\mathcal{H} = \mathcal{H}_0 \mathbf{I}_3 + \mathcal{W} \quad (1)$$

where $\mathcal{H}_0 = \mathcal{T}_N + \mathcal{V}_0$ is the unperturbed Hamiltonian of the electronic ground state of the SiH_4 within a harmonic approximation,

$$\mathcal{T}_N = -\frac{1}{2}\omega_1\frac{\partial^2}{\partial Q_1^2} - \frac{1}{2}\omega_2\left(\frac{\partial^2}{\partial Q_{2\theta}^2} + \frac{\partial^2}{\partial Q_{2\epsilon}^2}\right) - \frac{1}{2}\sum_{i=3}^4\omega_i\left(\frac{\partial^2}{\partial Q_{i\xi}^2} + \frac{\partial^2}{\partial Q_{i\eta}^2} + \frac{\partial^2}{\partial Q_{i\zeta}^2}\right) \quad (2)$$

and

$$\mathcal{V}_0 = \frac{1}{2}\omega_1 Q_1^2 + \frac{1}{2}\omega_2(Q_{2\theta}^2 + Q_{2\epsilon}^2) + \frac{1}{2}\sum_{i=3}^4\omega_i(Q_{i\xi}^2 + Q_{i\eta}^2 + Q_{i\zeta}^2) \quad (3)$$

The change of electronic energy upon ionization is expressed by the electronic Hamiltonian matrix with \mathcal{W} in eq 1 given by^{5,54}

$$\begin{aligned} \mathcal{W} &= (E_0 + \kappa_1 Q_1)\mathbf{e}_\alpha + \lambda_2(Q_{2\theta}\mathbf{e}_\theta + Q_{2\epsilon}\mathbf{e}_\epsilon) \\ &+ \sum_{i=3}^4\mu_i(Q_{i\xi}\mathbf{t}_\xi + Q_{i\eta}\mathbf{t}_\eta + Q_{i\zeta}\mathbf{t}_\zeta) \\ &+ \frac{1}{2}[\gamma_1 Q_1^2 + \gamma_2(Q_{2\theta}^2 + Q_{2\epsilon}^2) \\ &+ \sum_{i=3}^4\gamma_i(Q_{i\xi}^2 + Q_{i\eta}^2 + Q_{i\zeta}^2)]\mathbf{e}_\alpha \\ &+ \frac{1}{2}\lambda_{22}[(Q_{2\epsilon}^2 - Q_{2\theta}^2)\mathbf{e}_\theta + Q_{2\theta}Q_{2\epsilon}\mathbf{e}_\epsilon] \\ &+ \sum_{i=3}^4\mu_{ii}^{t_2}(Q_{i\eta}Q_{i\xi}\mathbf{t}_\xi + Q_{i\xi}Q_{i\zeta}\mathbf{t}_\eta + Q_{i\zeta}Q_{i\eta}\mathbf{t}_\zeta) \\ &+ \frac{1}{4}\sum_{i=3}^4\mu_{ii}^e(2Q_{i\zeta}^2 - Q_{i\xi}^2 - Q_{i\eta}^2)\mathbf{e}_\theta \\ &+ \sqrt{3}(Q_{i\xi}^2 - Q_{i\eta}^2)\mathbf{e}_\epsilon] \\ &+ \sum_{i=3}^4b_{2i}\left[\left(-\frac{1}{2}Q_{2\theta} + \frac{\sqrt{3}}{2}Q_{2\epsilon}\right)Q_{i\xi}\mathbf{t}_\xi \right. \\ &\left. + \left(-\frac{1}{2}Q_{2\theta} - \frac{\sqrt{3}}{2}Q_{2\epsilon}\right)Q_{i\eta}\mathbf{t}_\eta + Q_{2\theta}Q_{i\zeta}\mathbf{t}_\zeta\right] \\ &= \begin{pmatrix} \mathcal{W}_{11} & \mathcal{W}_{12} & \mathcal{W}_{13} \\ \mathcal{W}_{21} & \mathcal{W}_{22} & \mathcal{W}_{23} \\ \mathcal{W}_{31} & \mathcal{W}_{32} & \mathcal{W}_{33} \end{pmatrix} \end{aligned} \quad (4)$$

where \mathbf{e}_ω , \mathbf{e}_θ , and \mathbf{e}_ϵ and \mathbf{t}_ξ , \mathbf{t}_η , and \mathbf{t}_ζ are the matrices containing appropriate coupling coefficients, which are defined in the space of $|\xi\rangle$, $|\eta\rangle$, and $|\zeta\rangle$ of functions for the triply degenerate state at the reference geometry, along with the totally symmetric (a_1) and components of the doubly degenerate (e) and triply degenerate (t_2) vibrational modes. The six matrices, as appear above, are given by^{11,55}

$$\begin{pmatrix} 1 & 0 & 0 \\ 0 & 1 & 0 \\ 0 & 0 & 1 \end{pmatrix}, \begin{pmatrix} -\frac{1}{2} & 0 & 0 \\ 0 & -\frac{1}{2} & 0 \\ 0 & 0 & 1 \end{pmatrix}, \begin{pmatrix} \frac{\sqrt{3}}{2} & 0 & 0 \\ 0 & -\frac{\sqrt{3}}{2} & 0 \\ 0 & 0 & 0 \end{pmatrix}, \\ \begin{pmatrix} 0 & 0 & 0 \\ 0 & 0 & 1 \\ 0 & 1 & 0 \end{pmatrix}, \begin{pmatrix} 0 & 0 & 1 \\ 0 & 0 & 0 \\ 1 & 0 & 0 \end{pmatrix}, \text{ and } \begin{pmatrix} 0 & 1 & 0 \\ 1 & 0 & 0 \\ 0 & 0 & 0 \end{pmatrix}$$

Thus, the various elements of the matrix Hamiltonian in eq 4 are as follows:

$$\begin{aligned} \mathcal{W}_{11} &= E_0 + \kappa_1 Q_1 + \lambda_2\left(-\frac{1}{2}Q_{2\theta} + \frac{\sqrt{3}}{2}Q_{2\epsilon}\right) \\ &+ \frac{1}{2}[\gamma_1 Q_1^2 + \gamma_2(Q_{2\theta}^2 + Q_{2\epsilon}^2) \\ &+ \sum_{i=3}^4\gamma_i(Q_{i\xi}^2 + Q_{i\eta}^2 + Q_{i\zeta}^2)] \\ &+ \frac{1}{2}\lambda_{22}\left(\frac{1}{2}Q_{2\theta}^2 - \frac{1}{2}Q_{2\epsilon}^2 + \sqrt{3}Q_{2\theta}Q_{2\epsilon}\right) \\ &+ \frac{1}{4}\sum_{i=3}^4\mu_{ii}^e(2Q_{i\xi}^2 - Q_{i\eta}^2 - Q_{i\zeta}^2) \end{aligned} \quad (5a)$$

$$\begin{aligned} \mathcal{W}_{22} &= E_0 + \kappa_1 Q_1 + \lambda_2\left(-\frac{1}{2}Q_{2\theta} - \frac{\sqrt{3}}{2}Q_{2\epsilon}\right) \\ &+ \frac{1}{2}[\gamma_1 Q_1^2 + \gamma_2(Q_{2\theta}^2 + Q_{2\epsilon}^2) \\ &+ \sum_{i=3}^4\gamma_i(Q_{i\xi}^2 + Q_{i\eta}^2 + Q_{i\zeta}^2)] \\ &+ \frac{1}{2}\lambda_{22}\left(\frac{1}{2}Q_{2\theta}^2 - \frac{1}{2}Q_{2\epsilon}^2 - \sqrt{3}Q_{2\theta}Q_{2\epsilon}\right) \\ &+ \frac{1}{4}\sum_{i=3}^4\mu_{ii}^e(2Q_{i\eta}^2 - Q_{i\xi}^2 - Q_{i\zeta}^2) \end{aligned} \quad (5b)$$

$$\begin{aligned} \mathcal{W}_{33} &= E_0 + \kappa_1 Q_1 + \lambda_2 Q_{2\theta} + \frac{1}{2}[\gamma_1 Q_1^2 + \gamma_2(Q_{2\theta}^2 + Q_{2\epsilon}^2) \\ &+ \sum_{i=3}^4\gamma_i(Q_{i\xi}^2 + Q_{i\eta}^2 + Q_{i\zeta}^2)] \\ &+ \frac{1}{2}\lambda_{22}(-Q_{2\theta}^2 + Q_{2\epsilon}^2) \\ &+ \frac{1}{4}\sum_{i=3}^4\mu_{ii}^e(2Q_{i\zeta}^2 - Q_{i\xi}^2 - Q_{i\eta}^2) \end{aligned} \quad (5c)$$

$$\mathcal{W}_{12} = \mathcal{W}_{21} = \sum_{i=3}^4(\mu_i Q_{i\zeta} + \mu_{ii}^{t_2} Q_{i\xi} Q_{i\eta} + b_{2i} Q_{2\theta} Q_{i\zeta}) \quad (5d)$$

$$\begin{aligned} \mathcal{W}_{13} &= \mathcal{W}_{31} \\ &= \sum_{i=3}^4\left[\mu_i Q_{i\eta} + \mu_{ii}^{t_2} Q_{i\xi} Q_{i\zeta} + b_{2i}\left(-\frac{1}{2}Q_{2\theta} - \frac{\sqrt{3}}{2}Q_{2\epsilon}\right)Q_{i\eta}\right] \end{aligned} \quad (5e)$$

$$\begin{aligned} \mathcal{W}_{23} &= \mathcal{W}_{32} \\ &= \sum_{i=3}^4 \left[\mu_i Q_{i\varepsilon} + \mu_{ii}^t Q_{ii} Q_{i\varepsilon} + b_{2i} \left(-\frac{1}{2} Q_{2\theta} + \frac{\sqrt{(3)}}{2} Q_{2\varepsilon} \right) Q_{i\varepsilon} \right] \end{aligned} \quad (\text{Sf})$$

The diagonal elements present the diabatic potential energies of the three components of this electronic state whereas the off-diagonal elements are the corresponding couplings. The vertical ionization energy of the \tilde{X}^2T_2 electronic state of SiH_4^+ is denoted by E_0 . In turn, the linear coupling parameter of the totally symmetric a_1 vibrational mode is given by κ_1 , and the linear JT coupling parameters for doubly degenerate e and triply degenerate t_2 vibrational modes are denoted by λ_2 and μ_{ij} , respectively. Note that γ_1, γ_2 , and γ_i are the diagonal second-order parameters for the a_1 , e, and t_2 vibrations, respectively. The diagonal second-order parameters (γ_i) actually take care the frequency change due to an electronic transition from ground \tilde{X}^1A_1 electronic state of SiH_4 to the cationic \tilde{X}^2T_2 state along those vibrational modes, respectively. Additionally, b_{2i} represents the bilinear JT coupling parameters that arise due to coupling between the vibrational modes of e and t_2 symmetry. In turn, λ_{22} , μ_{ii}^e , and μ_{ii}^t refer to the quadratic JT coupling constants resulting from the nontotally symmetric tensor convolutions of the $e \times e$ and $t_2 \times t_2$ symmetrized direct products, respectively. Numerical values of all the above coupling parameters are determined by performing extensive ab initio electronic structure calculations (see below).

Dynamical Observables. The dynamical variables are reported by examining the vibronic energy level spectrum of the \tilde{X}^2T_2 electronic manifold of SiH_4^+ using the Hamiltonian constructed above. The intensity, $P(E)$, of the vibronic band is calculated by the Fermi's golden rule

$$P(E) = \sum_v |\langle \Psi_v^f | \hat{T} | \Psi_0^i \rangle|^2 \delta(E - E_v^f + E_0^i) \quad (6)$$

where $|\Psi_v^f\rangle$ represents the eigenstates of the vibronic Hamiltonian with energy E_v^f and $|\Psi_0^i\rangle$ is the initial ground vibronic state of the neutral molecule with energy E_0^i . \hat{T} is the operator that describes the interaction of the electrons with the external radiation, and E is the electron binding energy (ionization energy). The initial vibronic state

$$|\Psi_0^i\rangle = |\Phi_0\rangle |\chi_0^0\rangle \quad (7)$$

is represented as a product of the diabatic electronic ($|\Phi_0\rangle$) and vibrational ($|\chi_0^0\rangle$) components. The latter is the eigenfunction of the unperturbed reference Hamiltonian, H_0 . It should be noted that in the final vibronic state, $|\Psi_v^f\rangle$, the scattering wave function of the outgoing electron is missing. Similarly, the kinetic energy of the outgoing electron is missing in the Einstein condition of eq 6. In fact, the determination of the correct wave function of the final vibronic state is actually an intricate problem due to the fact that the scattering state belongs to the kinetic energy of the outgoing wave which behaves as a plane wave at an asymptotic distance but for shorter electron distances is modified due to interaction with the cation, a topic that is actually an active research area in nonadiabatic electron-scattering theory. It should also be noted that the calculation of vibronic intensities close to the ionization threshold poses an additional intricacy by the fact that it should verify the Wigner threshold law.⁵⁶ In the present case, we have used Franck–Condon factors to calculate the vibronic intensities for the \tilde{X}^2T_2 state of SiH_4^+ .

In a time-dependent picture, eq 6 can be related to a Fourier transform of the time autocorrelation function of the WP⁵⁷

$$P(E) \sim 2\text{Re} \int_0^\infty e^{iEt/\hbar} \langle 0 | \tau^\dagger e^{-i\mathcal{H}t/\hbar} \tau | 0 \rangle dt \quad (8)$$

$$\sim 2\text{Re} \int_0^\infty e^{iEt/\hbar} C^m(t) dt \quad (9)$$

The quantity, $C^m(t) = \langle \Psi^m(0) | \Psi^m(t) \rangle$, is the time autocorrelation function of the WP initially prepared on the m th electronic state. τ refers to the transition dipole matrix, $\tau^\dagger = (\tau^1, \tau^2, \tau^3)$, with $\tau^m = \langle \Phi_m | \hat{T} | \Phi_0 \rangle$; the dagger stands for transposed, and \tilde{X}_i ($i = 1-3$) for the various degenerate potential sheets. As discussed above, we assume that the ejected electron does not correlate with the electrons of the ion and the involved matrix elements are set to unity. This is in consistent with the applicability of the Franck–Condon approximation in a diabatic electronic basis.⁵⁷ The partial spectra are calculated by propagating WPs for three different initial conditions and convoluted them together to yield the final composite vibronic spectrum.

In a time-dependent method an appropriate WP is first prepared in the final electronic state of the cation and then propagated with the aid of the time-dependent Schrödinger equation, $i\hbar\partial_t|\Psi_v\rangle = \mathcal{H}|\Psi_v\rangle$. The autocorrelation function, $C^m(t)$, of the WP is recorded in time and Fourier transformed to finally calculate the vibronic spectrum via eqs 8 and 9. The WP propagation is carried out by employing the efficient MCTDH algorithm⁴⁷⁻⁵¹ best suited for full quantum mechanical simulation of multistate and multimode problems like the present one. The multiset ansatz of the MCTDH algorithm allows a combination of vibrational degrees of freedom to effectively reduce the dimensionality problem. The WP associated with each electronic state is described using a different set of single particle functions (SPFs). When the nuclear degrees of freedom f are combined, p numbers of particles are formed ($p < f$). The variables for the p sets of SPFs are defined in terms of the single- or multidimensional coordinates of a particle. The operational principles of the MCTDH algorithm are discussed in detail in the literature,^{50,51} and we do not reiterate here.

Determination of Coupling Parameters. An accurate determination of various coupling parameters of the Hamiltonian is crucial to provide a strong basis for the dynamics calculation. To accomplish this task, the adiabatic electronic PESs of the \tilde{X}^2T_2 electronic state of SiH_4^+ are calculated along the dimensionless normal coordinates of the electronic ground state (\tilde{X}^1A_1) of neutral SiH_4 . The geometry optimization and calculation of harmonic vibrational frequencies of SiH_4 at the calculated equilibrium geometry of its electronic ground state (1A_1) are carried out at the second-order Møller–Plesset perturbation (MP2) level of theory by employing the correlation-consistent polarized valence triple- ζ (cc-pVTZ) basis set of Dunning⁵⁸ with the Gaussian-03 program.⁵⁹ The equilibrium geometry of ground state SiH_4 (\tilde{X}^1A_1) belongs to the T_d symmetry point group. Its optimized value is defined by $r_{\text{SH}} = 1.4770 \text{ \AA}$, in good accord with the experimental counterpart of 1.4798 \AA .⁶⁰ The harmonic frequencies (ν_i , $i = 1-9$) of the vibrational modes of the electronic ground state of SiH_4 are obtained by diagonalizing the MP2 force field and are given in Table 1 along with their fundamental values available from experiment.⁶¹ In turn, the normal displacement coordinates (from their equilibrium value at $Q = 0$), referred to here as Q_i for the i th vibrational mode, are obtained by multiplying the mass weighted normal coordinates with $(\nu_i)^{1/2}$ (in atomic units).⁶²

Table 1. Description of the Vibrational Modes of the Electronic Ground State of SiH₄ Computed at the MP2/cc-pVTZ Level of Theory^a

mode	frequency		predominant	
	this work	exp ⁶¹	nature	coordinates
$\nu_1(a_1)$	0.28486	0.27004	symmetric stretching	Q_1
$\nu_2(e)$	0.12448	0.12101	symmetric scissoring	$Q_{2\theta}, Q_{2e}$
$\nu_3(t_2)$	0.28577	0.27165	asymmetric stretching	$Q_{3\zeta}, Q_{3\eta}, Q_{3\zeta}$
$\nu_4(t_2)$	0.11786	0.11295	asymmetric scissoring	$Q_{4\zeta}, Q_{4\eta}, Q_{4\zeta}$

^aThough the theoretical frequencies are harmonic in nature, the experimental ones are fundamentals. All values are in electronvolts.

The diabatic coupled surfaces of the \tilde{X}^2T_2 electronic manifold of SiH₄⁺ are constructed by calculating the associated adiabatic ab initio energies along one and two dimensions in the normal mode coordinate space of the neutral SiH₄. In the endeavor to obtain the energies at high accuracy, care should be taken to account for electron correlation. To achieve such a requirement, complete-active-space self-consistent-field (CASSCF) calculation has been performed to optimize the molecular orbitals followed by multireference configuration-interaction (MRCI) calculations to account for the dynamical correlation using the full-valence-complete-active-space (FVCAS) wave function as reference. In this, the Si 1s, 2s, and 2p core orbitals have been kept closed but are optimized in the CASSCF step. However, in the MRCI calculations, such core orbitals were treated as frozen. The FVCAS reference wave function involves therefore seven correlated electrons in eight active orbitals, amounting to a total of 2352 configuration state functions. For the basis set, we have selected the cc-pVTZ basis of Dunning,⁵⁸ with the calculations being carried out using the Molpro package.⁶³ The eigenvalues of the above 3×3 diabatic Hamiltonian matrix (excluding the kinetic energy of the nuclei) have then been fitted to the adiabatic ab initio ionization energies by a least-squares procedure to derive numerically the various coupling parameters and hence the adiabatic PESs. We note that the eigenvalues of a 3×3 matrix generically depend nonlinearly on the fitting parameters even if they appear linearly on each individual matrix element. The fit has then been carried out without great difficulty by using the Levenberg–Marquardt algorithm.⁶⁴ It should be noted that there is no analytic solution for the present least-squares problem.

In the first step, the vertical ionization energy of the three sheets of the \tilde{X}^2T_2 electronic manifold is calculated by distorting the initial T_d geometry along the i th vibrational mode (keeping others at their equilibrium value) at intervals of 0.5 over the range of $0 \leq |Q_i| \leq 6$. The PESs obtained were then used to determine the various coupling parameters of the one-dimensional (1D) potential of the model Hamiltonian constructed above. In the second step, the vertical ionization energies are calculated for the simultaneous displacements of two components of e mode coordinate, two components of the t_2 mode coordinates, and one component of the e and t_2 mode coordinates. Note that in all three cases both coordinates are varied by an equal amount. Then all coupling parameters of the vibronic Hamiltonian in eq 4 were fitted to ab initio energies obtained from the above distorted geometries along the diagonal of this two-dimensional (2D) nuclear coordinate subspace, with the coupling parameters estimated from the 1D cuts as initial guess. The optimum fitted parameters are given in Table 2.

Table 2. Coupling Parameters in Eqs 1–5f As Obtained from CASSCF/MRCI Calculations^a

mode	$\kappa_1/(\lambda_2/\mu_i)$	$\gamma_{(1/2)/i}$	λ_{22}/μ_{ii}^b	μ_{ii}^e	b_{2i}
$\nu_1(a_1)$	0.2167	−0.0009			
$\nu_2(e)$	0.3348	−0.0426	−0.0252		
$\nu_3(t_2)$	0.2482	−0.0091	0.0019	−0.0201	−0.0236
$\nu_4(t_2)$	0.2513	−0.0472	0.0100	0.0239	0.0545
IP	12.77044				
IP(exp) ³⁸	12.82				

^aThe vertical ionization potential (IP) of the \tilde{X}^2T_2 electronic state of SiH₄⁺ is also given along with its experimental value. All values are in electronvolts.

RESULTS AND DISCUSSION

Adiabatic Potential Energy Surfaces. An examination of the topography of adiabatic PESs of the \tilde{X}^2T_2 electronic state of SiH₄⁺ near the JT conical intersection is performed here. As pointed out in the previous section, the model vibronic Hamiltonian (eqs 1–5f) is designed to reproduce the ab initio adiabatic PESs under T_d symmetry within the harmonic approximation. The various parameters of the Hamiltonian have been obtained by a least-squares fit of its eigenvalues to the ab initio data points. Resulting 1D cuts of the multidimensional PESs along the dimensionless normal coordinate of a given vibrational mode keeping others at their equilibrium values, $Q = 0$, are shown in Figures 1 and 2. In each plot, the points represent

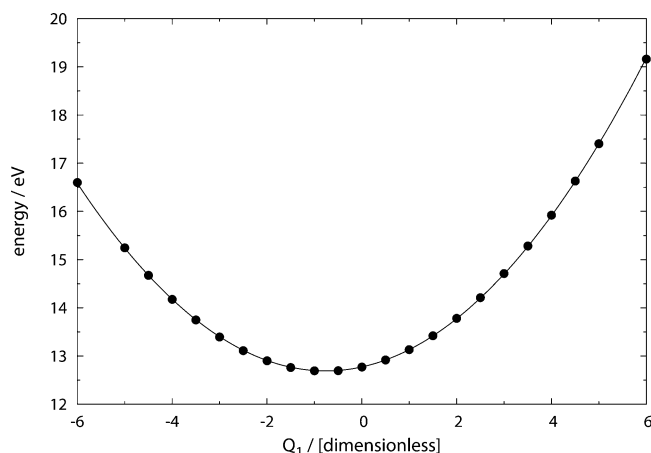


Figure 1. Adiabatic potential energies of the \tilde{X}^2T_2 electronic state of SiH₄⁺ along the dimensionless normal coordinate of the totally symmetric vibrational mode ν_1 . Energy of the ground electronic state of SiH₄ (\tilde{X}^1A_1) at equilibrium configuration ($Q = 0$) is set to zero. The present vibronic model is shown by the solid line and the computed ab initio data by the solid dots.

the computed ab initio adiabatic potential energies, and the curves superimposed on them the fitted model.

In Figure 1, a 1D cut of the multidimensional potential energy hypersurface of the \tilde{X}^2T_2 electronic state is plotted along the totally symmetric (a_1) stretching vibrational mode (ν_1). It can be seen that the degeneracy of \tilde{X}^2T_2 electronic manifold remains unaffected upon distortion along the symmetric vibrational mode. However, it alters the nuclear dynamics by tuning the position and energy of the minimum of the JT conical intersection which occurs at $Q_1^0 = -0.7631$ with an energy of $\mathcal{V}_{\min}^{(c)} \sim 12.6877$ eV. Similarly, the 1D ab initio potential energy cuts along both the components ($Q_{2\theta}$ and Q_{2e}) of the doubly

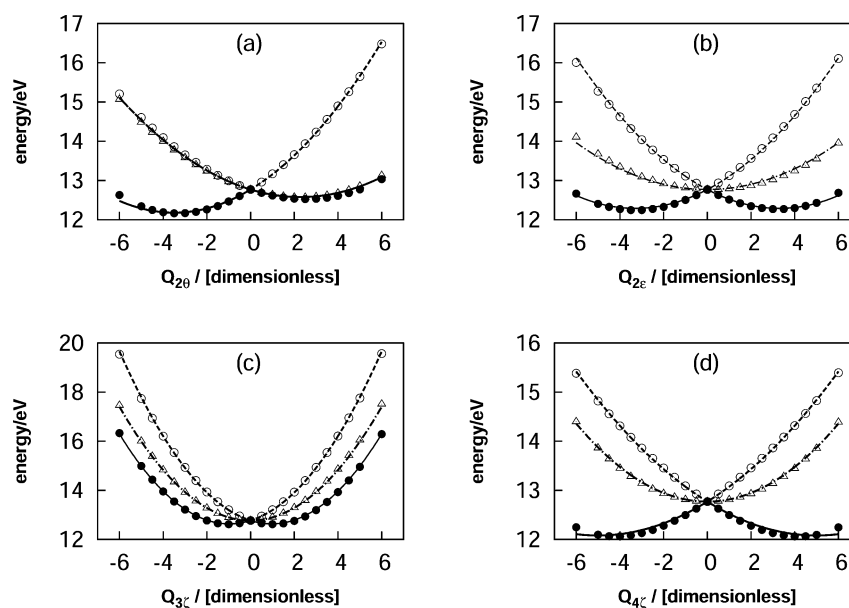


Figure 2. Same as in Figure 1 along both the components (θ and ϵ) of e and ζ component of t_2 vibrational modes, respectively.

degenerate (e) scissoring mode (ν_2) are illustrated in panels a and b of Figure 2. The two sets of potential energy cuts shown in panels a and b of this figure reveal that the nuclear displacements along the $Q_{2\epsilon}$ component splits the triply degenerate \tilde{X}^2T_2 electronic manifold into three nondegenerate electronic states, whereas the one along the $Q_{2\theta}$ component yields a partial lifting, namely one doubly degenerate and one nondegenerate electronic states. Thus, it is necessary to fit them simultaneously and the best fitted results are depicted in panels b and a of Figure 2, in the above order. The global root-mean-square error estimated for the final fit is $\sim 3.9 \times 10^{-2}$ eV. The electronic degeneracy of the \tilde{X}^2T_2 state is also split when distortion is along the triply degenerate vibrational modes ν_3 and ν_4 , and this splitting leads to three states altogether. We note that any of the three vibrational components (Q_ϵ , Q_θ , and Q_ζ) lift the triple electronic degeneracy in a way similar to that for a given t_2 mode, and hence we have shown the potential energy cuts only along one component for the sake of brevity. The resulting potential energy cuts along the Q_ζ component of the vibrational modes ν_3 and ν_4 are illustrated in panels c and d of Figure 2, respectively. It can be seen that the current model mimics well all ab initio data points. Within a first-order coupling approach, the JT stabilization energy due to the formation of new minima on the lowest adiabatic sheet of the JT split \tilde{X}^2T_2 state along the doubly degenerate ν_2 vibrational mode is predicted to be $\lambda_2^2/2\omega_2 \sim 0.4488$ eV whereas the same due to both triply degenerate ν_3 and ν_4 vibrational modes amounts to $\sum_{i=3}^4 2\mu_i^2/3\omega_i \sim 0.5009$ eV. Therefore, in addition to the totally symmetric a_1 vibrational mode, all three JT active vibrations ($\nu_2-\nu_4$) are also expected to have a pivotal role on the nuclear dynamics of this electronic manifold.

In the above we have considered the ab initio adiabatic potential energy cuts along only a single normal mode coordinate and fitted them by diagonalizing the modeled diabatic electronic Hamiltonian with high accuracy. We will then examine the potential energy cuts along the diagonal of the 2D subspace of nuclear coordinates obtained from the simultaneous displacement of two JT active e and t_2 normal mode coordinates. There are three possible combinations of coordinates that manifest nonvanishing JT couplings on a 2D subspace: (i) the two

coordinates correspond to the two components of the e mode; (ii) both belong to one t_2 mode (the possibility of combining the other t_2 mode has been ignored for simplicity); (iii) one belongs to the e mode and the other to the t_2 mode. The full matrix is fitted to the calculated ab initio data points, and the results are shown in Figures 3 and 4. The adiabatic potential energy cuts shown in different panels of Figure 3 correspond to the simultaneous displacement of two component coordinates belonging to the e and t_2 vibrations, cases i and ii. A comparison of these three diagonal cuts shows that the lowest adiabatic sheet of the JT split \tilde{X}^2T_2 state is relatively flat for the displacement coordinates of two bending vibrations (ν_2 and ν_4) compared to the stretching vibration (ν_3). A similar observation applies to the lowest adiabatic sheet of panels b and d of Figure 4. The flat nature of the lowest adiabatic sheet of the \tilde{X}^2T_2 electronic state illustrated in the various panels of Figures 3 and 4 is probably a manifestation of the floppiness of the title radical cation, which should then be primarily due to ν_2 and ν_4 vibrations. Therefore special care should be taken in the matrix representation of the adiabatic energies along the coordinate space of those two large amplitude vibrations. A qualitative scheme to account for this has been suggested in our previous work.¹⁹ Accordingly, we first investigate the nuclear motion underlying the first vibronic band of SiH_4^+ with the above established model PESs. Then we will vary the slope of the adiabatic PESs (linear JT coupling parameter) along those two bending vibrational modes (ν_2 and ν_4) up to $\pm 10\%$ with a view to examine their role on the floppiness of the molecule via agreement of the simulated versus experimental spectra within the current QVC model Hamiltonian.

Vibronic Spectra. The photoelectron spectrum underlying the \tilde{X}^2T_2 electronic manifold of SiH_4^+ obtained by employing the above modeled diabatic vibronic Hamiltonian (eqs 1–5f) is presented in Figure 5 along with the spectrum recorded from the He I photoelectron spectroscopy experiment by Potts and Price.³⁸ It is already discussed in the previous section that all the nine vibrational modes may have important role on the structure of this photoelectron band. We follow therefore the nuclear dynamics simultaneously on the three diabatically coupled sheets of the \tilde{X}^2T_2 electronic manifold including all the nine vibrational

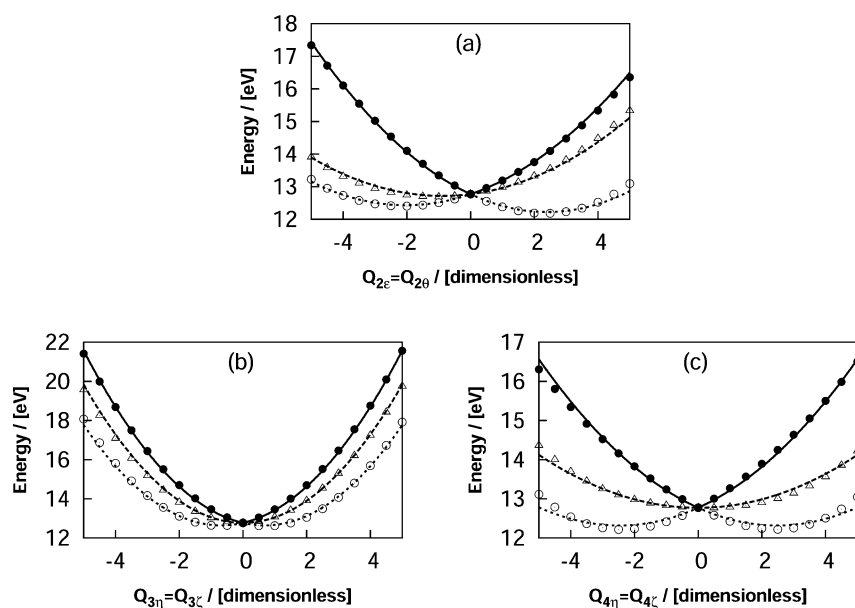


Figure 3. Same as in Figure 1 along the simultaneous displacement of two coordinates of e and t_2 vibrational modes, respectively.

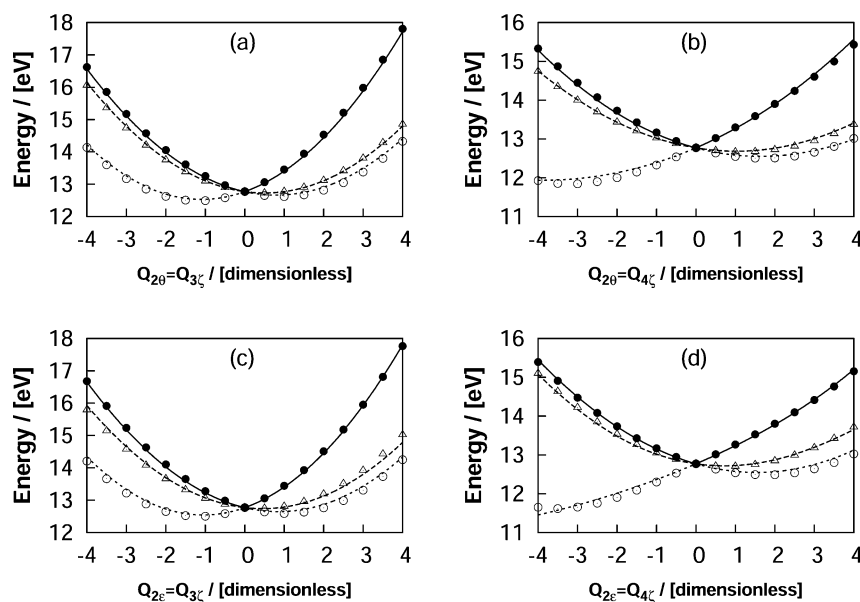


Figure 4. Same as in Figure 1 along the simultaneous displacement of two coordinates of one component of the e mode and one component of the t_2 vibrational modes.

degrees of freedom. This leads to an Hamiltonian matrix of huge dimension, and the associated Schrödinger equation cannot be solved by diagonalizing it. Thus, we solve the Schrödinger equation by propagating WPs within a time-dependent framework using the MCTDH algorithm^{47–51} and obtain the eigenvalue spectrum. The required normal mode combinations and sizes of the primitive and single particle bases to prepare the WP for propagation in this \tilde{X}^2T_2 electronic manifold of SiH_4^+ are given in Table 3. Three calculations are carried out by initially preparing the WP separately on each component of the \tilde{X}^2T_2 electronic manifold. The WP in each calculation is propagated for 150 fs. The time autocorrelation functions from the above three calculations are combined, damped with an exponential function to account for experimental line broadening effects, e^{-t/τ_r} (with $\tau_r = 33$ fs), and finally Fourier transformed to calculate the vibronic band of this \tilde{X}^2T_2 electronic state. The value of τ_r

used in the damping function corresponds to a convolution of the vibronic line spectrum with a Lorentzian function of 30 meV fwhm. The simulated spectrum envelope displayed in Figure 5, is in good agreement with the experimental spectrum.³⁸ Both the characteristic line structure, spectral intensity and the width of the vibronic band are well reproduced by the present QVC scheme.

In the following, we examine the effect of various coupling terms on the shape of spectral envelope underlying the \tilde{X}^2T_2 vibronic band of SiH_4^+ . To arrive at a better understanding of such an effect, we proceed systematically by dropping some of the coupling terms in the theoretical calculations, with the results being presented in Figure 6. The results shown in panel a of this figure are obtained by retaining only linear coupling terms of all the vibrational degrees of freedom, including the quadratic term of the totally symmetric ν_1 vibrational mode. This leads to the

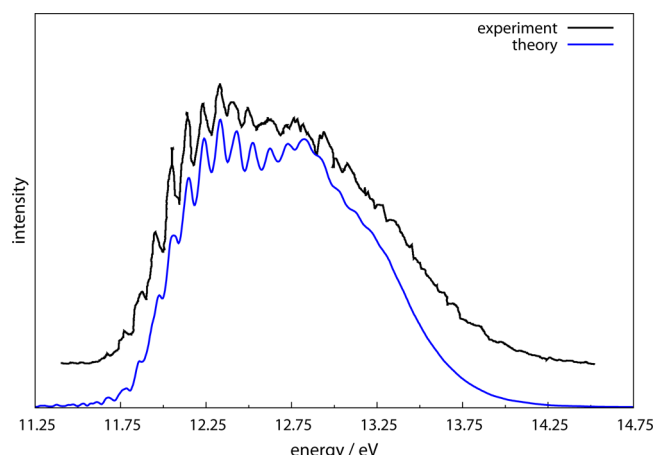


Figure 5. Vibronic band of the \tilde{X}^2T_2 electronic state of SiH_4^+ . The intensity (in arbitrary units) is plotted along the energy (relative to minimum of the \tilde{X}^1A_1 state of SiH_4) of the final vibronic states.

Table 3. Normal Mode Combinations and Sizes of Both the Primitive and Single-Particle Bases Used in the WP Propagation within the MCTDH Framework in the Coupled Electronic Manifold Using the Complete Vibronic Hamiltonian of Eqs 1–5f^a

normal modes	primitive basis	SPF basis	figure
$(\nu_1, \nu_{2g}, \nu_{4g})$	(8, 35, 30)	[12,10,8]	5
$(\nu_{2g}, \nu_{4g}, \nu_{4g})$	(35, 30, 30)	[12,12,12]	
$(\nu_{3g}, \nu_{4g}, \nu_{3g})$	(10, 10, 10)	[9,9,9]	

^aThe first column denotes the vibrational degrees of freedom (DOF) which are combined to particles. Second column gives the number of primitive basis functions for each DOF. The third column gives the number of single particle functions (SPFs) for each JT splitted electronic state.

well established linear vibronic coupling scheme augmented by the diagonal quadratic term of ν_1 vibration. The theoretical results thus obtained underestimate strongly the irregular spectral excitations and are mismatched in their intensities. Next we have considered all quadratic coupling terms of the JT active $\nu_2 - \nu_4$ vibrations for the nuclear dynamics simulations. However, for a more systematic exposition, the intermode coupling terms (b_{23} and b_{24}) between the JT active vibrational modes of e and t_2 symmetry are suppressed here and the results are displayed in panel b of Figure 6. As shown, the theoretical results are in good agreement with the vibronic structure, spectral intensity, and overall width of the experimentally recorded photoelectron spectrum.³⁸ Similarly, the theoretical results obtained from the complete QVC Hamiltonian (eqs 1–5f) are shown in panel c of this figure for a better comparison with the above two results. A careful look at the three spectra clearly reveals that the vibrational structure obtained by dropping the intermode JT couplings shows visible, although not drastic, differences when compared with the results obtained from the complete QVC Hamiltonian. Conversely, the various panels of Figure 6 pinpoint the pivotal role of the quadratic vibronic couplings of the JT active vibrations in interpreting the complicated vibronic structure and intensities. It therefore cements the necessity of their inclusion for a reliable description of the dynamical JT effect in the \tilde{X}^2T_2 manifold of SiH_4^+ .

It is also of interest to compare the dominant vibrational progressions predicted from the current model Hamiltonian with

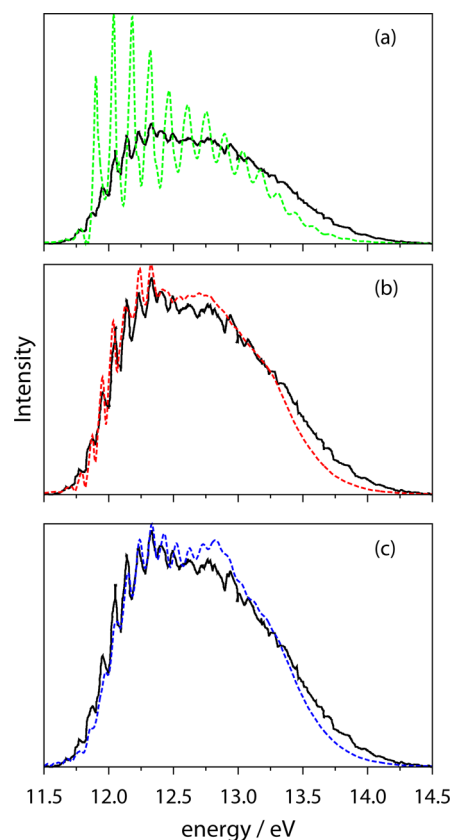


Figure 6. Comparison of various approximate theoretical results (dash lines) for the \tilde{X}^2T_2 vibronic band of SiH_4^+ with the experimental photoelectron spectrum (solid line).³⁸ (a) Spectrum calculated by employing LVC Hamiltonian augmented by diagonal quadratic coupling parameter of totally symmetric ν_1 vibration only. (b) Spectrum simulated by using present QVC Hamiltonian but excluding intermode couplings. (c) Spectrum obtained from the present full QVC Hamiltonian. The intensity is the same as in Figure 5.

the ones available from experiment. For such a comparison, we first construct various reduced-dimensionality models in terms of a_1 , e, and t_2 vibrational modes and examine the vibrational levels separately. These results help us to understand the role of various vibrational modes in the complex vibronic structure of the \tilde{X}^2T_2 electronic state of SiH_4^+ . The vibronic energy eigenvalues are obtained by diagonalizing the Hamiltonian matrix using the Lanczos algorithm.⁵² The fundamental and overtones up to second order are excited for the ν_1 mode. A corresponding peak spacing of ~ 0.2844 eV can be estimated from the calculated partial spectrum for the ν_1 vibration. A similar spectrum due to the ν_2 vibrational mode reveals an extended progression of this vibrational mode due to its large JT coupling (Table 2). A line spacing of ~ 0.1154 eV is predicted. The partial spectrum due to both t_2 vibrations has also been calculated. The intense lines are ~ 0.3342 and ~ 0.0665 eV spaced relative to the band origin corresponding to the frequency of the ν_3 and ν_4 vibrational modes, respectively. However, the JT activity of the triply degenerate asymmetric scissoring mode ν_4 is stronger than the triply degenerate asymmetric stretching mode ν_3 . Thus, ν_4 scissoring mode forms the dominant progression underlying the partial spectrum obtained due to t_2 modes. On analyzing the fine structure in the low-energy region of experimentally recorded first photoelectron band of the title molecule, Pullen et al.³⁷ has found nine equally spaced vibrational peaks up to 12.46 eV and

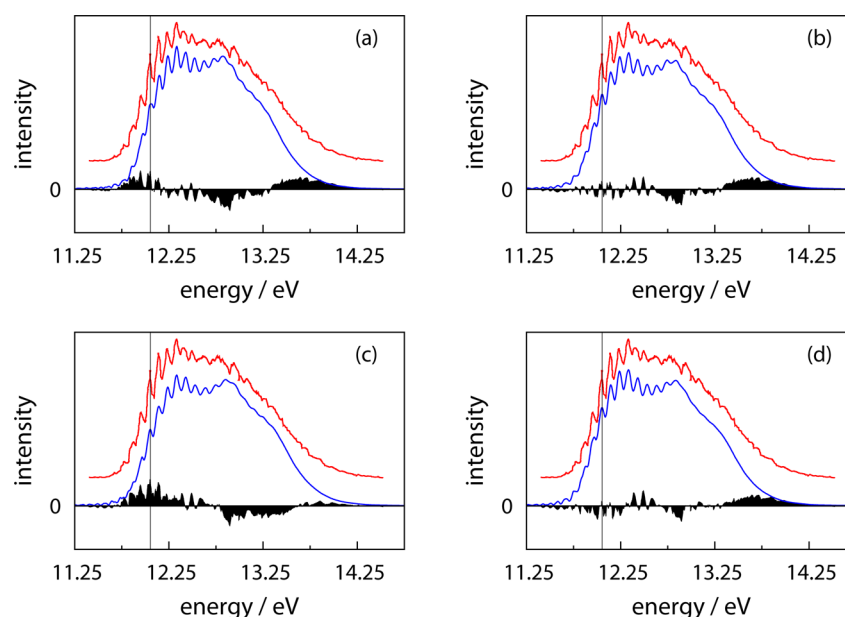


Figure 7. Vibronic band of the \tilde{X}^2T_2 electronic state of SiH_4^+ ; the intensity is the same as in Figure 5. (a) Spectrum computed from the present QVC model Hamiltonian. (b) As in (a) but adjusting the linear coupling parameters by +5% for both ν_2 and ν_4 mode. (c) As in (a) but adjusting the linear coupling parameters by +10% for both ν_2 and ν_4 modes. (d) As in (a) but adjusting the linear coupling parameters by −10% for the ν_1 mode, +5% for ν_2 , +10% for ν_3 , and +5% for ν_4 , respectively.

estimated their separation is ~ 0.10 eV (~ 807 cm^{-1}). In turn, Potts and Price³⁸ found a well-defined regular vibrational pattern in the low-energy side of their better resolved photoelectron spectrum with an average vibrational peak spacing of ~ 0.093 eV (~ 750 cm^{-1}). They assigned these vibronic energy levels as due to the ν_2 vibration. As mentioned above, our estimate based on reduced-dimensional calculations predict a peak spacing of ~ 0.1154 eV (~ 931 cm^{-1}) in the vibrational progressions caused by the ν_2 mode and thus found to overestimate the experimentally observed one. However, the average peak spacing of ~ 0.0938 eV (~ 756 cm^{-1}), predicted from the nearly converged full-dimensional calculations are in excellent agreement with the experimental estimate of Potts and Price.³⁸ Additionally, the reduction of line spacing in the full-dimensional calculations compared to its reduced-dimensional counterpart reveal the importance of intermode coupling effects on the vibronic structure of this photoelectron band.

At this point, we address the possible appearance of hot band transitions. This is an issue of photoelectron spectra at room temperatures when the molecule suffers large distortions. Due to the huge number of Franck–Condon overlap integrals that require consideration to study such hot band transitions, its simulation can be computationally tedious and unaffordable. Thus, it has not been attempted here. Note, though, that the present study aims at a comparison with the He I photoelectron spectrum of silane recorded by Potts and Price³⁸ who, to our knowledge, have not observed any such hot band transitions in their work.

We compare now the above results in relation to those found for CH_4^+ .^{18,19} Although the first photoelectron band observed for both methane and silane are similar in their general trends, the overall width of the band progressively decreases in the latter due to the smaller JT coupling effect. It has already been established in our previous investigations^{18,19} as well as in the present study that the vibrational progressions in the low-energy side of the first photoelectron band of the above

molecules are dominated by the doubly degenerate bending vibrational mode (ν_2). However, the JT coupling associated with this in SiH_4^+ is found to be ~ 0.3348 eV whereas the same in CH_4^+ is estimated as ~ 0.6617 eV. As a result, a well-resolved regular vibrational pattern appears for SiH_4^+ in the low-energy wing, which contrasts with the highly diffuse and broad spectrum envelope of the first photoelectron band of CH_4 .

As we have already noted, the low-frequency ν_2 and ν_4 modes should be primarily responsible for the aforementioned large amplitude motions in SiH_4^+ . Indeed, such motions manifest in a molecule through the location and/or energy of the minima available in the associated PESs, i.e., through the topography of the latter. A qualitative way to deal with this problem in the present scheme will then be by varying the slope (linear coupling term) of the corresponding adiabatic PESs, because such parameters dictate the position and/or energy of the minima along the relevant vibrational coordinates. First, we investigate the impact on the first vibronic band of the title radical cation by varying the linear JT coupling parameters by up to $\pm 10\%$ of the corresponding theoretical values. We start by considering all four combinations (resulting from varying ν_2 and ν_4) with a $\pm 5\%$ change in the linear JT coupling parameters and simulate the vibronic spectra of the resulting \tilde{X}^2T_2 electronic manifold of SiH_4^+ . The differences between the calculated and experimental spectra so obtained are shown in Figure 7 as impulses in solid black. Among the four calculated spectra, we judge the best agreement between theory and experiment to be found for the combination where the linear JT parameter is increased by 5% of its calculated value for both the ν_2 and ν_4 modes. This judgment is done by calculating the integrated absolute deviation (IAD) of intensity per electronvolt between the calculated and experimental spectra. The best result so obtained in comparison to the observed spectrum is shown in panel b of Figure 7 and a quantitative estimate of its IAD value against the experimental recordings³⁸ is found to be ~ 2.04 in arbitrary units. Of course, for the above comparison, we had to make a one-to-one correspondence of the peaks. Because this is hardly possible,

we have chosen a prominent peak as potential candidate as the reference. This is indicated by the vertical line in Figure 7, with the same procedure being followed for all other panels of this figure.

Panel a illustrates the amount of disagreement obtained from the present theoretical QVC model Hamiltonian with the experimental recordings without any adjustment of the coupling parameters of the Hamiltonian. The IAD value is now estimated to be ~ 2.58 . Subsequently, we varied the linear JT coupling parameters for these two modes by $\pm 10\%$ and calculated the spectra for all the four possible combinations. Again, the best agreement has been found for increasing both ν_2 and ν_4 mode parameters with the corresponding IAD value being ~ 2.53 . The result is shown in panel c of Figure 7. This indicates a $\sim 1.84\%$ enhancement in the agreement with experiment for the 10% increase of the linear JT coupling parameters of ν_2 and ν_4 . However, the improvement becomes $\sim 20.75\%$ when only a 5% increase is considered. Of course, we are dealing with a multimode JT problem, and hence all four relevant vibrational modes are entangled with each other. Because a fully optimized search is out of the question, we have tentatively varied the linear coupling terms of all four vibrational modes by $\pm 10\%$ and $\pm 5\%$. The best result is predicted by decreasing the ν_1 linear coupling parameters by 10% while increasing the ν_2 , ν_3 , and ν_4 ones by 5%, 10%, and 5%. This simulation is depicted in panel d of Figure 7. The IAD value in this case is

Table 4. Integrated Absolute Deviation (IAD, in Arbitrary Units) per Electronvolt of the Calculated Spectra Relative to Their Experimental Counterparts in CH_4^+ ¹⁹ and SiH_4^+ ^a

model	CH_4^+	SiH_4^+	% improvement
QVC ^b	2.19	2.58	
c	2.05		6.44
d	2.41		−9.98
e	1.96		10.52
f		2.04	20.75
g		2.53	1.84
h		1.83	29.13

^aThe first column indicates the model Hamiltonian, and the fourth gives the percentage of improvement due to the changes in the linear JT coupling. ^bQuadratic vibronic coupling Hamiltonian. ^cAs in a but adjusting the linear couplings by -5% for ν_2 and $+5\%$ for the ν_4 mode. ^dAs in a but with -10% for ν_2 and $+10\%$ for the ν_4 mode. ^eAs in a but with -10% for ν_1 , -5% for ν_2 , $+10\%$ for ν_3 , and $+5\%$ for the ν_4 mode. ^fAs in a but with $+5\%$ for both ν_2 and ν_4 modes. ^gAs in a but with $+10\%$ for both ν_2 and ν_4 modes. ^hAs in a but with -10% for ν_1 , $+5\%$ for ν_2 , $+10\%$ for ν_3 , and $+5\%$ for the ν_4 mode. See text.

estimated to be ~ 1.83 . This leads to a $\sim 29.14\%$ enhancement.³⁸ A summary of the whole set of results is shown in Figure 7 and Table 4. For comparison, we have included the corresponding values obtained in our previous work for CH_4^+ , because they have not been reported there. The results show a marginal improvement for SiH_4^+ vs CH_4^+ .

CONCLUDING REMARKS

A detailed theoretical analysis of multimode JT interactions on the triply degenerate lowest electronic state (\tilde{X}^2T_2) of SiH_4^+ has been carried out. For this, the model Hamiltonian has been built from extensive ab initio electronic structure calculations, with first principles simulations being then utilized to examine the electronic nonadiabatic effects on the nuclear dynamics. Specifically,

the quantum chemical calculations have been performed with a high-level multireference wave function, with the underlying PESs being represented through one- and two-dimensional cuts in terms of the normal-mode coordinates of SiH_4 . The various coupling parameters of the QVC Hamiltonian were determined by fitting the eigenvalues of the matrix Hamiltonian to the ab initio calculated adiabatic PESs. In turn, the vibronic energy level structure of SiH_4^+ has been examined at various levels of theoretical approximation via diagonalization of the Hamiltonian matrix. Similarly, the assignment of vibrational structures of the first vibronic band has been made and a comparison with the available experimental results presented.^{37,38} Time-dependent quantal methods have finally been carried out to simulate the nonadiabatic nuclear motion. As discussed above, the theoretical predictions are found to be in very good agreement with the experimental data.³⁸ We summarize below the major findings: (a) the highly diffuse and overlapping first photoelectron band is due to strong JT activity of all three degenerate vibrational modes; (b) the quadratic vibronic couplings of the JT active vibrations are crucial in explaining the broadening and spectral intensities; (c) the ν_2 vibration yields the dominant progression in the low-energy region; (d) the intermode coupling effects are key for mimicking the experimental vibronic line spacing in the low-energy part of the photoelectron band; (e) the JT stabilization energies are ~ 0.4488 and ~ 0.5009 eV for the e and t_2 vibrations; (f) in striking contrast to CH_4^+ , the well-defined regular vibronic structure in the low-energy wing of the first vibronic band of SiH_4^+ can be attributed to the smaller JT coupling of the ν_2 vibrational mode.

AUTHOR INFORMATION

Corresponding Author

*A. J. C. Varandas: e-mail, varandas@qtvsl1.qui.uc.pt.

Notes

The authors declare no competing financial interest.

ACKNOWLEDGMENTS

This work is financed by FEDER through “Programa Operacional Factores de Competitividade - COMPETE” and national funds under the auspices of Fundação para a Ciência e a Tecnologia, Portugal (projects PTDC/QUI-QUI/099744/2008 and PTDC/AAC-AMB/099737/2008).

REFERENCES

- (1) Jahn, H. A.; Teller, E. Stability of Polyatomic Molecules in Degenerate Electronic States. I. Orbital Degeneracy. *Proc. R. Soc. London Ser. A* **1937**, *161*, 220–235, DOI: 10.1098/rspa.1937.0142.
- (2) Opik, U.; Pryce, M. H. L. Studies of the Jahn-Teller Effect. I. A Survey of the Static Problem. *Proc. R. Soc. London Ser. A* **1957**, *238*, 425–447, DOI: 10.1098/rspa.1957.0010. Longuet-Higgins, H. C.; Opik, U.; Pryce, M. H. L.; Sack, R. A. Studies of the Jahn-Teller Effect. II. The Dynamical Problem. *Proc. R. Soc. London Ser. A* **1958**, *244*, 1–16, DOI: 10.1098/rspa.1958.0022. Longuet-Higgins, H. C. *Adv. Spectrosc.* **1961**, *2*, 429–472.
- (3) Englman, R. *The Jahn-Teller Effect in Molecules and Crystals*; Wiley: New York, 1972.
- (4) Köppel, H.; Domcke, W.; Cederbaum, L. S. Multimode Molecular-dynamics Beyond the Born-Oppenheimer Approximation. *Adv. Chem. Phys.* **1984**, *57*, 59–246.
- (5) Bersuker, I. B. *The Jahn-Teller Effect*; Cambridge University Press, Cambridge, U.K., 2006. Bersuker, I. B. Modern Aspects of the Jahn-Teller Effect Theory and Applications To Molecular Problems. *Chem. Rev.* **2001**, *101*, 1067–1114, DOI: 10.1021/cr0004411.

- (6) Mahapatra, S. Quantum Non-adiabatic Dynamics Through Conical Intersections: Spectroscopy to Reactive Scattering. *Int. Rev. Phys. Chem.* **2004**, *23*, 483–512, DOI: 10.1080/01442350500037455.
- (7) Mahapatra, S. Excited Electronic States and Nonadiabatic Effects in Contemporary Chemical Dynamics. *Acc. Chem. Res.* **2009**, *42*, 1004–1015, DOI: 10.1021/ar800186s.
- (8) Varandas, A. J. C. Geometrical Phase Effect in Jahn-Teller Systems: Twofold Electronic Degeneracies and Beyond. *Chem. Phys. Lett.* **2010**, *487*, 139–146, DOI: 10.1016/j.cplett.2010.01.032.
- (9) Köppel, H.; Cederbaum, L. S.; Mahapatra, S. Theory of the Jahn-Teller Effect In *Handbook of High Resolution Spectroscopy*; Quack, M., Merkt, F., Eds.; Wiley: Chichester, U.K., 2011.
- (10) Sturge, M. D. In *Solid State Physics: Advances in Research and Applications*; Seitz, F., Turnbull, D., Ehrenreich, H., Eds.; Academic: New York, 1967; Vol. 20, pp 91.
- (11) Van Vleck, J. H. The Jahn-Teller Effect and Crystalline Stark Splitting for Clusters of the Form XY_6 . *J. Chem. Phys.* **1939**, *7*, 72–84, DOI: 10.1063/1.1750327.
- (12) Moffitt, W.; Thorson, W. Vibronic States of Octahedral Complexes. *Phys. Rev.* **1957**, *108*, 1251–1255, DOI: 10.1103/PhysRev.108.1251.
- (13) O'Brien, M. C. M. Dynamic Jahn-Teller Effect in an Orbital Triplet State Coupled to Both E_g and T_{2g} Vibrations. *Phys. Rev.* **1969**, *187*, 407–418, DOI: 10.1103/PhysRev.187.407.
- (14) Stoneham, A. M.; Lannoo, M. The Jahn-Teller Instability with Accidental Degeneracy. *J. Phys. Chem. Solids* **1969**, *30*, 1769–1777, DOI: 10.1016/0022-3697(69)90245-5.
- (15) Sakamoto, N. Vibronic Model Leading to Orthorhombic Jahn-Teller Distortions. *Phys. Rev. B* **1982**, *26*, 6438–6443, DOI: 10.1103/PhysRevB.26.6438.
- (16) Caner, M.; Engelman, R. Jahn-Teller Effect on a Triplet Due to Threefold Degenerate Vibrations. *J. Chem. Phys.* **1966**, *44*, 4054–4055, DOI: 10.1063/1.1726575.
- (17) Varandas, A. J. C.; Sarkar, B. Generalized Born-Oppenheimer Treatment of Jahn-Teller Systems in Hilbert Spaces of Arbitrary Dimension: Theory and Application to a Three-State Model Potential. *Phys. Chem. Chem. Phys.* **2011**, *13*, 8131–8135, DOI: 10.1039/C0CP02598D.
- (18) Opalka, D.; Domcke, W. High-Order Expansion of $T_2 \times t_2$ Jahn-Teller Potential-Energy Surfaces in Tetrahedral Molecules. *J. Chem. Phys.* **2010**, *132*, 154108 DOI: 10.1063/1.3382912.
- (19) Opalka, D.; Domcke, W. High-Order Expansion of $T_2 \times e$ Jahn-Teller Potential-Energy Surfaces in Tetrahedral Systems. *Chem. Phys. Lett.* **2010**, *494*, 134–138, DOI: 10.1016/j.cplett.2010.06.011.
- (20) Signorell, R.; Merkt, F. PFI-ZEKE Photoelectron Spectra of the Methane Cation and the Dynamic Jahn-Teller Effect. *Faraday Discuss.* **2000**, *115*, 205–208, DOI: 10.1039/A909272B.
- (21) Wörner, H. J.; Merkt, F. Jahn-Teller Effects in Molecular Cations Studied by Photoelectron Spectroscopy and Group Theory. *Angew. Chem., Int. Ed.* **2009**, *48*, 6404–6424, DOI: 10.1002/anie.200900526.
- (22) Mondal, T.; Varandas, A. J. C. The Jahn-Teller Effect in the Triply Degenerate Electronic State of Methane Radical Cation. *J. Chem. Phys.* **2011**, *135*, 174304 DOI: 10.1063/1.3658641.
- (23) Mondal, T.; Varandas, A. J. C. Quadratic Coupling Treatment of the Jahn-Teller Effect in the Triply-Degenerate Electronic State of CH_4^+ : Can One Account for Floppiness? *J. Chem. Phys.* **2012**, *137*, 214320 DOI: 10.1063/1.4768675.
- (24) Frey, R. F.; Davidson, E. R. Potential Energy Surfaces of CH_4^+ . *J. Chem. Phys.* **1988**, *88*, 1775–1785, DOI: 10.1063/1.454101.
- (25) Paddon-Row, M. N.; Fox, D. J.; Pople, J. A.; Houk, K. N.; Pratt, D. W. Dynamic Jahn-Teller Effect in Methane Radical Cation. Location of the Transition Structures for Hydrogen Scrambling and Inversion. *J. Am. Chem. Soc.* **1985**, *107*, 7696–7700, DOI: 10.1021/ja00311a078.
- (26) Arents, J.; Allen, L. C. Ab Initio Study of the Geometries, Jahn-Teller Distortions, and Electronic Charge Distribution in the CH_4^+ Ion. *J. Chem. Phys.* **1970**, *53*, 73–78, DOI: 10.1063/1.1673835.
- (27) Schmitt, J. P. M.; Greisser, P.; Krishnan, M.; De Rosny, G. Perrin. Production Mechanism and Reactivity of the SiH Radical in a Silane Plasma. *Chem. Phys.* **1984**, *84*, 281–293, DOI: 10.1016/0301-0104(84)85213-1.
- (28) Goldhaber, D. M.; Betz, A. L. Silane in IRC +10216. *Astrophys. J.* **1984**, *279*, L55 DOI: 10.1086/184255.
- (29) Robin, M. B. *Higher Excited States of Polyatomic Molecules*; Academic: New York, 1974; Vol. I.
- (30) Roberge, R.; Sandorfy, C. The Far Ultraviolet and He I Photoelectron Spectra of Alkyl and Fluorine Substituted Silane Derivatives. *J. Chem. Phys.* **1978**, *69*, 5105–5112, DOI: 10.1063/1.436456.
- (31) Hays, W. H.; Brown, F. C. Absorption by Some Molecular Gases in the Extreme Ultraviolet. *Phys. Rev. A* **1972**, *6*, 21–30, DOI: 10.1103/PhysRevA.6.21.
- (32) Schwarz, W. H. E. Continuous Change from Valence to Rydberg Type States. An Example of XUV Spectroscopy. *Chem. Phys.* **1975**, *9*, 157–164, DOI: 10.1016/0301-0104(75)80125-X.
- (33) Schwarz, W. H. E. Interpretation of the Core Electron Excitation Spectra of Hydride Molecules and the Properties of Hydride Radicals. *Chem. Phys.* **1975**, *11*, 217–228, DOI: 10.1016/0301-0104(75)80001-2.
- (34) Suto, M.; Lee, L. C. Quantitative Photoexcitation Study of SiH_4 in Vacuum Ultraviolet. *J. Chem. Phys.* **1986**, *84*, 1160–1164, DOI: 10.1063/1.450506.
- (35) Chantranupong, L.; Hirsch, G.; Buenker, R. J.; Dillon, M. A. Configuration Interaction Calculations of the Vertical Electronic Spectrum of Silane. *Chem. Phys.* **1993**, *170*, 167–175, DOI: 10.1016/0301-0104(93)80061-D.
- (36) Liotard, D.; Chaillet, M.; Dargelos, A. Theoretical Study of the Electronic Spectrum of SiH_4 . *J. Chem. Phys.* **1988**, *88*, 3848–3852, DOI: 10.1063/1.453886.
- (37) Koch, A.; Peyerimhoff, S. D. Multireference Configuration Interaction Calculations of the Vertical K-shell Excitation Spectrum of Di-fluoro-silane. *Chem. Phys.* **1993**, *172*, 21–32, DOI: 10.1016/0301-0104(93)80103-G.
- (38) Lampe, F. W. In *NATO ASI Series B Physics*; Ausloos, P., Ed.; Plenum: New York, 1974.
- (39) Perrin, J.; Lloret, A.; De Rosny, G.; Schmitt, J. P. M. Positive and Negative Ions in Silane and Disilane Multipole Discharges. *Int. J. Mass Spectrom. Ion Processes* **1984**, *57*, 249–281, DOI: 10.1016/0168-1176(84)85082-X.
- (40) Smith, D. M.; Martineau, P. M.; Davies, P. B. Infrared Laser Absorption Spectroscopy of the SiH_3^+ Cation. *J. Chem. Phys.* **1992**, *96*, 1741–1747, DOI: 10.1063/1.462129.
- (41) Pullen, B. P.; Carlson, T. A.; Moddeman, W. E.; Schweitzer, G. K.; Bull, W. E.; Grimm, F. A. Photoelectron Spectra of Methane, Silane, Germane, Methyl Fluoride, Difluoromethane, and Trifluoromethane. *J. Chem. Phys.* **1970**, *53*, 768–782, DOI: 10.1063/1.1674057.
- (42) Potts, A. W.; Price, W. C. The Photoelectron Spectra of Methane, Silane, Germane and Stannane. *Proc. R. Soc. London Ser. A* **1972**, *326*, 165–179, DOI: 10.1098/rspa.1972.0003.
- (43) Genuit, W.; Boerboom, A. J. H.; Gover, T. R. The ArI Photoionization Mass Spectrum of Silane: Observation of the SiH_4^+ Molecular Ion. *Int. J. Mass Spectrom. Ion Processes* **1984**, *62*, 341–344, DOI: 10.1016/0168-1176(84)87120-7.
- (44) Börlin, K.; Heinis, T.; Jungen, M. Photoionization Mass Spectrometry of Silane. *Chem. Phys.* **1986**, *103*, 93–100, DOI: 10.1016/0301-0104(86)85105-9.
- (45) Berkowitz, J.; Greene, J. P.; Cho, H.; Ruscic, B. Photoionization Mass Spectrometric Studies of S_nH_n ($n=1-4$). *J. Chem. Phys.* **1987**, *86*, 1235–1248, DOI: 10.1063/1.452213.
- (46) Gordon, M. S.; Gano, D. R.; Binkley, J. S.; Frisch, M. J. Thermal Decomposition of Silane. *J. Am. Chem. Soc.* **1986**, *108*, 2191–2195, DOI: 10.1021/ja00269a011.
- (47) Power, D.; Brint, P.; Spalding, T. A Gaussian 80 (6–21G) Study of the Species SiH_n ($n=1-4$) and SiH_m^+ ($m=1-5$): Some Comments on the Electron Impact Mass Spectrum of Silane. *J. Mol. Struct. THEOCHEM* **1984**, *108*, 81–92, DOI: 10.1016/0166-1280(84)80103-7.
- (48) Caballol, R.; Catala, J. A.; Prolet, J. M. Jahn-Teller Distortions in XH_4^+ Radical Cations ($X=Si, Ge, Sn$). an Ab initio CI Study. *Chem. Phys. Lett.* **1986**, *130*, 278–284, DOI: 10.1016/0009-2614(86)80469-9.

- (45) Pople, J. A.; Curtiss, L. A. Theoretical Thermochemistry. 2. Ionization Energies and Proton Affinities of AH_n Species ($A = C$ to F and Si to Cl); Heats of Formation of their Cations. *J. Phys. Chem.* **1987**, *91*, 155–162, DOI: 10.1021/j100285a035.
- (46) De Proft, F.; Geerlings, P. Ab initio and Density Functional Study of the Jahn-Teller Distortion in the Silane Radical Cation. *Chem. Phys. Lett.* **1996**, *262*, 782–788, DOI: 10.1016/S0009-2614(96)01152-9.
- (47) Worth, G. A.; Beck, M. H.; Jäckle, A.; Meyer, H.-D. *The MCTDH Package*, Version 8.2; University of Heidelberg, Heidelberg, Germany, 2000. Meyer, H.-D. *The MCTDH Package*, Version 8.3; University of Heidelberg, Heidelberg, Germany, 2002. See <http://www.pci.uni-heidelberg.de/tc/usr/mctdh/>.
- (48) Meyer, H.-D.; Manthe, U.; Cederbaum, L. S. The Multiconfigurational Time-dependent Hartree Approach. *Chem. Phys. Lett.* **1990**, *165*, 73–78, DOI: 10.1016/0009-2614(90)87014-I.
- (49) Manthe, U.; Meyer, H.-D.; Cederbaum, L. S. Wave-Packet Dynamics Within the Multiconfiguration Hartree Framework: General Aspects and Application to NOCl. *J. Chem. Phys.* **1992**, *97*, 3199–3213, DOI: 10.1063/1.463007.
- (50) Beck, M. H.; Jäckle, A.; Worth, G. A.; Meyer, H.-D. The Multiconfiguration Time-dependent Hartree (MCTDH) Method: a Highly Efficient Algorithm for Propagating Wavepackets. *Phys. Rep.* **2000**, *324*, 1–105, DOI: 10.1016/S0370-1573(99)00047-2.
- (51) *Multidimensional Quantum Dynamics: MCTDH Theory and Applications*; Meyer, H.-D., Gatti, F., Worth, G. A., Eds.; Wiley-VCH: New York, 2009.
- (52) Cullum, J.; Willoughby, R. *Lanczos Algorithms for Large Symmetric Eigenvalue Problems*; Birkhäuser: Boston, 1985; Vols. I and II.
- (53) Köppel, H.; Domcke, W. In *Encyclopedia of Computational Chemistry*, Schleyer, P. V. R., Ed.; Wiley: New York, 1998; p 3166.
- (54) Ceulemans, A.; Beyens, D.; Vanquickenborne, L. G. Symmetry Aspects of Jahn-Teller Activity: Structure and Reactivity. *J. Am. Chem. Soc.* **1984**, *106*, 5824–5837, DOI: 10.1021/ja00332a012.
- (55) Bersuker, I. B.; Polinger, V. Z. The Second Order $T-e-t_2$ Problem in the Jahn-Teller Effect Theory. A New Type of Adiabatic Potential Minima and Inversion (tunneling) Splitting. *Phys. Lett. A* **1973**, *44*, 495–496, DOI: 10.1016/0375-9601(73)90990-0. Bersuker, I. B.; Polinger, V. Z. *Sov. Phys. JETP* **1974**, *39*, 1023.
- (56) Wigner, E. P. On the Behavior of Cross Sections Near Thresholds. *Phys. Rev.* **1948**, *73*, 1002–1009, DOI: 10.1103/PhysRev.73.1002.
- (57) Domcke, W.; Köppel, H.; Cederbaum, L. S. Spectroscopic Effects of Conical Intersections of Molecular Potential Energy Surfaces. *Mol. Phys.* **1981**, *43*, 851–875, DOI: 10.1080/00268978100101721.
- (58) Dunning, T. H., Jr. Gaussian Basis Sets for Use in Correlated Molecular Calculations. I. The Atoms Boron Through Neon and Hydrogen. *J. Chem. Phys.* **1989**, *90*, 1007–1023, DOI: 10.1063/1.456153.
- (59) Frisch, M. J.; et al. *Gaussian 03*, revision B.05; Gaussian, Inc.: Pittsburgh, PA, 2003.
- (60) Boyd, D. R. J. Infrared Spectrum of Trideuterosilane and the Structure of the Silane Molecule. *J. Chem. Phys.* **1955**, *23*, 922–926, DOI: 10.1063/1.1742148.
- (61) Cardona, M. Vibrational Spectra of Hydrogen in Silicon and Germanium. *Phys. Status Solidi (b)* **1983**, *118*, 463–481, DOI: 10.1002/pssb.2221180202.
- (62) Wilson, E. B., Jr.; Decius, J. C.; Cross, P. C. *Molecular Vibrations*; McGraw-Hill: New York, 1955.
- (63) Werner, H.-J.; Knowles, P. J.; Lindh, R.; Manby, F. R.; Schütz, M.; et al. *MOLPRO*, version 2010.1, a package of ab initio programs, see <http://www.molpro.net>.
- (64) Levenberg, K. *Quart. Appl. Math.* **1944**, *2*, 164–168. Marquardt, D. W. An Algorithm for Least-Squares Estimation of Nonlinear Parameters. *SIAM J. Appl. Math.* **1963**, *11*, 431–441, DOI: 10.1137/0111030.